Atomic position and the chemical state of an active Sn dopant for Sn-doped β-Ga_2O_3(001)

Yuhua Tsai,[1,2] Masaaki Kobata,[3] Tatsuo Fukuda,[3] Hajime Tanida,[3] Toru Kobayashi,[3] and Yoshiyuki Yamashita[1,2,*]

[1]*National Institute for Materials Science, Tsukuba, Ibaraki 305-0044, Japan.*
[2]*Department of Applied Chemistry, Faculty of Engineering, Kyushu University, Motooka 744, Fukuoka 819-0395, Japan*
[3]*Materials Sciences Research Center, Japan Atomic Energy Agency (JAEA), 1-1-1, Kouto, Sayo, Hyogo 679-5148, Japan*

*E-mail: YAMASHITA.Yoshiyuki@nims.go.jp

ABSTRACT

We investigated the atomic position and the chemical state of an active Sn dopant for Sn-doped β-Ga_2O_3(001) using x-ray absorption near the edge structure (XANES) and hard x-ray photoelectron spectroscopy (HAXPES). We found that the Sn dopant had only one chemical state, which was a Sn^{4+} oxidation state. The bond length around the Sn dopant atom became longer due to the relaxation effect after the Sn dopant insertion. Comparison of the experimental and simulated XANES spectra showed that the octahedral Ga substitutional site in the β-Ga_2O_3(001) is an active Sn dopant site.

MAIN TEXT

In recent years, gallium oxide (Ga_2O_3) has gained significant attention as an ultra-wide bandgap semiconductor because of its bandgap of around 5 eV, its high thermal stability, and the availability of large-scale Ga_2O_3 single crystal wafers. Such superior properties of Ga_2O_3 can be applied to the field of electronic and photonic devices, such as high-power transistors, deep-UV photodetectors, and sensors. For Ga_2O_3, there are five crystal polymorphs: α-, β-, δ-, γ-, and κ-Ga_2O_3, among which β-Ga_2O_3 has received the most attention due to its highest thermal stability.[1-7]

In general, precise control of carrier density, mobility, and resistivity is essential for the application of β-Ga_2O_3-based devices in electronic and optoelectronic fields.[8,9] Dopants in β-Ga_2O_3 can enhance the electrical properties of materials and optimize device performance.[1,10-12] Previous studies showed that Sn is used as an n-type dopant in β-Ga_2O_3 to control electrical properties.[11-15] Ohira et al. found that Sn is uniformly dispersed in β-Ga_2O_3 and suggested that it may be substituted in the Ga site in the β-Ga_2O_3 lattice.[15,16] There are two inequivalent Ga atomic sites in β-Ga_2O_3: octahedral (Octa) and tetrahedral (Tetra).[11,12] However, it has not been clarified how many chemical states exist in Sn-doped β-Ga_2O_3 and which of the substitutional Octa and/or Tetra sites is the active dopant one. Determining the atomic structure and the chemical state of active Sn dopant in β-Ga_2O_3 is a necessary step. Once both have been clarified, we can create a strategy to increase the activation of the Sn dopant. This approach might increase the industrial relevance of Sn-doped β-Ga_2O_3 for cost-sensitive applications, such as field effect transistors and gas sensors.

In the present study, we investigated the atomic position and the chemical state of an active site for Sn-doped β-Ga_2O_3 using x-ray absorption near the edge structure (XANES), extended x-ray absorption fine structure (EXAFS) and hard x-ray photoelectron spectroscopy (HAXPES).

The Sn-doped β-Ga_2O_3(001) substrate used in this study was purchased from Novel Crystal Technology, Inc. The Sn-doped β-Ga_2O_3 single crystal was grown using the edge-defined film-fed growth process. Ga_2O_3 powder was used as the source material. We placed the source powder in an iridium crucible surrounded by a radio frequency (RF) induction coil and added tin dioxide (SnO_2) powder to the Ga_2O_3 powder as the Sn dopant source. Heating was performed using an RF induction coil to reach a melting point of β-Ga_2O_3 (1800°C under atmospheric pressure). A mixture of 98% N_2 and 2% O_2 gas at 1 atm pressure was used for the growth process[5,17,18] whose details were described elsewhere.[5] The carrier concentration of the Sn dopant was also obtained from Novel Crystal Technology, Inc. Electrochemical capacitance-voltage measurements estimated the carrier concentration to be 1.1×10^{19} cm^{-3}.[5] Sn metal foil (Nilaco Corporation), SnO powder, and SnO_2 powder (Fujifilm Wako Pure Chemical Corp.) were used as reference samples.

HAXPES measurements for the reference samples (Sn metal foil, SnO powder, and SnO_2 powder) were done using PHI Quantes (ULVAC-PHI). Monochromatic Cr Kα (5414.9 eV) was used as incident x-rays for HAXPES. Its energy resolutions were set to 1.11 eV. The take-off angle was set to 90° (the surface normal). We used Au film to estimate the Fermi level and perform the energy calibration. We employed a neutralizer to avoid the charging effect. Note that for the PHI Quantes, it was very difficult to measure the Sn $2p_{3/2}$ signal for the Sn-doped β-Ga_2O_3 because of the quite low intensity. Thus, we used SPring-8 (third generation synchrotron institute) to obtain the Sn $2p_{3/2}$ HAXPES spectrum for the Sn-doped β-Ga_2O_3.

HAXPES, XANES, and EXAFS measurements were performed at BL22XU at SPring-8.[19-22] For the HAXPES measurements, the incident photon energy was 8 keV, and the energy resolution was set to 340 meV. We used a SCIENTA-OMICRON EW4000 with a large-acceptance-angle as an electron analyzer.[23] Kirkpatrick-Baez focusing mirrors were used and the beam size at the sample position was ~30 μm × ~30 μm (horizontal × vertical). The take-off angle (TOA) was set to 89° (the surface normal is 90°). Au film was used to estimate the Fermi level and perform the energy calibration. A neutralizer was employed to avoid the charging effect. The Sn K-edge XANES and EXAFS measurements were made using the fluorescence yield and the transmission yields. We measured them with a 19-element high-purity germanium detector (Mirion Technologies (Canberra) KK) and an ionization chamber.[21] The beam's spot-size at the sample position was ~0.4 μm × ~0.5 μm (horizontal × vertical).[22] The energy range for the EXAFS measurements was 29,000 eV to 29,480 eV with energy steps of 1.0 eV.

We used FEFF9[24,25] for the XANES simulations and employed ~ 350 atoms, full multiple scattering, a self-consistent field, Hedin-Lundqvist (HL) exchange-correlation potential, and the final-state effect (Z+1 approximation).[26,27] In the simulated XANES spectra, the absorption edges were shifted by 39 eV to correct the edge energy to the experimental value.[28-30]

Figure 1 shows the Sn $2p_{3/2}$ HAXPES spectra for the Sn-doped β-Ga_2O_3(001), the Sn metal foil, the SnO powder, and the SnO_2 powder. We used Voight function (convolution of Lorentzian and Gaussian functions) for peak fitting after removal of the background of the Shirley function.[31-33] For the peak fitting, we fixed 1.7 eV of full width at half maximums (FWHM) of the Lorentzian componet for all the samples. Only one peak is observed at 3932.3±0.05 eV for the Sn-doped β-Ga_2O_3(001), indicating that the dopant Sn atom exhibits a single chemical state. In the Sn metal HAXPES spectrum, a peak is observed at 3928.8±0.05 eV. For the SnO powder, a peak is seen at 3931.0±0.05 eV in the HAXPES spectrum. The SnO_2 powder HAXPES spectrum shows a peak position at 3930.5±0.05 eV. The FWHMs of the Gausiian componet for the Sn-doped β-Ga_2O_3(001), the Sn metal foil, the SnO powder, and the SnO_2 powder were 1.67, 1.84, 2.15, 1.94 eV, respectivety. Since the Sn dopant atom exhibits a similar peak position to the SnO powder and the SnO_2 powder, its chemical state may be due to an oxidation state. In addition, since the Sn dopant may be due to the oxidation state, it might be attributed to the Ga substitution site (Sn_{Ga}). Note that the Sn $2p_{3/2}$ spectrum measured for SnO powder shows higher binding energy level than that for SnO_2 powder.[34] Considering the oxidation states of 2^+ for SnO and 4^+ for SnO_2, the peak position of SnO_2 powder should show higher binding energy level. We think this phenomenon might be attributed to the final state effect for the photoelectron formation process.[35,36]

Figure 2(a) shows the Sn K-edge XANES spectra for the Sn-doped β-Ga_2O_3(001), the Sn metal foil, and the SnO powder and the SnO_2 powders. Figure 2(b) shows the edge positions of the Sn metal, the SnO powder, the SnO_2 powder, and the Sn-doped β-Ga_2O_3(001) whose edge positions are observed at 29191.0±1, 29194.9±1, 29198.5±1, and 29198.0±1 eV, respectively. These edge energies were determined by the first derivative peak of the leading edge for the Sn K-edge XANES spectra.[37] Figure 2(c) shows the oxidation state as a function of the energy of the absorption edge for Sn K-edge, which was obtained from the previous estimations.[38,39] This figure indicates that the Sn-doped β-Ga_2O_3(001) exhibits ~ Sn^{4+} state. Since relative chemical shifts were caused by changes in the oxidation state,[40] the dopant Sn atom might be attributed to the tetravalent state (Sn^{4+}) for the Sn-doped β-Ga_2O_3(001). Therefore, the Sn dopant state in the HAXPES spectrum (Fig. 1(a)) might be assigned to the Sn^{4+} oxidation state.

We employed EXAFS measurements to investigate changes in the interatomic bond length around the Sn dopant atom for Sn-doped β-Ga_2O_3(001). Figures 3(a) and (b) show the EXAFS spectrum and the oscillations for the Sn-doped β-Ga_2O_3(001). The range in k-space was chosen at 2.5–7 $Å^{-1}$. Figure 3(c) shows the Fourier transforms of the k^2-weighted EXAFS and the fitting result of the Octa Sn_{Ga} site. The fitting was performed using ARTEMIS software, and the reliability factor was set to 0.026 under k^2 weights in the 2.5–7 $Å^{-1}$ k range.[41,42] The fitting range was chosen at 1–2.2 Å in r-space. The amplitude reduction factor was set to 0.8. From the fitting results, the nearest Sn-O distance was estimated to be 2.03 Å, indicating that the bond length of the Sn-O of the Octa Sn_{Ga} site became longer than the Octa site of the non-doped β-Ga_2O_3.[43] This bond extension may be due to the relaxation effect of the Sn dopant insertion into the non-doped β-Ga_2O_3. We were unable to fit the Fourier transforms of the k^2-weighted EXAFS well in the case of the Tetra Sn_{Ga} site (Fig. 3(d)). Therefore, the Octa Sn_{Ga} site might be attributed to the active dopant site for Sn-doped β-Ga_2O_3.

Figure 4 shows the experimental (Fig. 4(a)) and simulated XANES spectra for the Octa Sn_{Ga} (Fig. 4(b)) and Tetra Sn_{Ga} (Fig. 4(c)) sites. Note that for the simulated Octa Sn_{Ga} XANES, a Sn-O bond length of 2.03 Å was employed. In the experimental XANES spectrum (Fig. 4(a)), a main strong sharp peak is observed at 29204.1 eV. In addition, a weak shoulder at 29221.9 eV and a broad component centered at 29252.7 eV are observed. (see arrows in Fig. 4(a)) For the Octa Sn_{Ga} simulated XANES spectrum (Fig. 4(b)), a main strong sharp peak and a weak shoulder are observed at 29202.3 and 29219.5 eV, respectively. In addition, a broad component centered at 29262.1 eV is observed. (see arrows in Fig. 4(b)) The simulated XANES spectrum of the Tetra Sn_{Ga} structure (Fig. 4(c)) has two broad peaks at 29204.9 and 29223.2 eV and two weak components centered at 29267.9 and 29291.1 eV. (see arrows in Fig. 4(c)) From the comparison of the experimental and simulated XANES spectra, we found that the simulated XANES spectrum of the Octa Sn_{Ga} has a similar shape to the experimental XANES spectrum for Sn-doped β-Ga_2O_3(001). This result is supported by the density functional theory where Octa Sn_{Ga} exhibits a more stable site than Tetra Sn_{Ga}.[44] In contrast, the simulated XANES spectrum for the Tetra Sn_{Ga} site does not explain the experimental spectrum. Thus, we conclude that Octa Sn_{Ga} is the atomic structure of the Sn dopant site for Sn-doped β-Ga_2O_3(001).

In conclusion, we used HAXPES, XANES, and EXAFS to clarify the chemical state and the atomic position of the Sn dopants for Sn-doped β-Ga_2O_3(001). From HAXPES, we found that the Sn dopant showed one chemical state. From the Sn K-edge XANES spectrum, the Sn dopant exhibited a Sn^{4+} oxidation state and the atomic position of the Sn dopant was attributed to Octa Sn_{Ga}. Preparing the low resistivity at the surface of Ga_2O_3 based device is very important issue to avoid the formation of the high resistivity when the surfaces contact with other materials such as metals. Our results indicate that the surface should be covered fully by the Octa Sn_{Ga} site to form the low resistivity. Thus, the low resistivity at the surface might be realized by adding adequate amount of the Sn dopant to the surface.

Acknowledgments

This work was supported by the Advanced Research Infrastructure for Materials and Nanotechnology in Japan (ARIM Japan) of the Ministry of Education, Culture, Sports, Science and Technology (MEXT), Japan (Grant No. JPMXP1223AE0025) and the Shared-Use Program of JAEA Facilities (Proposal No. 2023B-E09). The synchrotron radiation experiments were performed at SPring-8 JAEA (QST) beamline BL22XU with the approval of the Japan Synchrotron Radiation Research Institute (JASRI) (Proposal Nos.2023B3742, 2023B3731, and 2023B3732).

Reference

1. Pearton, J. Yang, P.H. Cary, F. Ren, J. Kim, M.J. Tadjer, and M.A. Mastro, Applied Physics Reviews **5**, 011301 (2018).
2. J. Zhang, J. Shi, D.-C. Qi, L. Chen, and K.H. Zhang, APL Materials **8**, 020906 (2020).
3. D. Guo, Q. Guo, Z. Chen, Z. Wu, P. Li, and W. Tang, Materials Today Physics **11**, 100157 (2019).
4. H. Dong, H. Xue, Q. He, Y. Qin, G. Jian, S. Long, and M. Liu, Journal of Semiconductors **40**, 011802 (2019).
5. A. Kuramata, K. Koshi, S. Watanabe, Y. Yamaoka, T. Masui, and S. Yamakoshi, Japanese Journal of Applied Physics **55**, 1202A2 (2016).
6. N.S. Jamwal and A. Kiani, Nanomaterials **12**, 2061 (2022).
7. N. Liu, H. Lin, W. Zhang, and J. Ye, Materials Science in Semiconductor Processing **168**, 107858 (2023).
8. X. Chen, F. Ren, S. Gu, and J. Ye, Photonics Research **7**, 381 (2019).
9. K.D. Chabak, K.D. Leedy, A.J. Green, S. Mou, A.T. Neal, T. Asel, E.R. Heller, N.S. Hendricks, K. Liddy, A. Crespo, N.C. Miller, M.T. Lindquist, N.A. Moser, R.C. Fitch, D.E. Walker, D.L. Dorsey, and G.H. Jessen, Semiconductor Science and Technology **35**, 013002 (2019).
10. S. Müller, H. von Wenckstern, D. Splith, F. Schmidt, and M. Grundmann, Physica Status Solidi (a) **211**, 34 (2013).

11. S.C. Siah, R.E. Brandt, K. Lim, L.T. Schelhas, R. Jaramillo, M.D. Heinemann, D. Chua, J. Wright, J.D. Perkins, C.U. Segre, R.G. Gordon, M.F. Toney, and T. Buonassisi, Applied Physics Letters **107**, 252103 (2015).
12. H. Arima-Osonoi, K. Yamazaki, R. Simura, T. Sugawara, K. Yubuta, K. Sugiyama, and A. Yoshiasa, Journal of Crystal Growth **570**, 126223 (2021).
13. M. Higashiwaki, K. Sasaki, A. Kuramata, T. Masui, and S. Yamakoshi, Physica Status Solidi (a) **211**, 21 (2013).
14. M. Baldini, M. Albrecht, A. Fiedler, K. Irmscher, R. Schewski, and G. Wagner, ECS Journal of Solid State Science and Technology **6**, Q3040 (2016).
15. S. Ohira, N. Suzuki, N. Arai, M. Tanaka, T. Sugawara, K. Nakajima, and T. Shishido, Thin Solid Films **516**, 5763 (2008).
16. C.-C. Wang, B.-C. Lee, F.-S. Shieu, and H.C. Shih, Chemical Physics Letters **753**, 137624 (2020).
17. M.J. Tadjer, J.A. Freitas, J.C. Culbertson, M.H. Weber, E.R. Glaser, A.L. Mock, N.A. Mahadik, K. Schmieder, E. Jackson, J.C. Gallagher, B.N. Feigelson, and A. Kuramata, Journal of Physics D: Applied Physics **53**, 504002 (2020).
18. M. Higashiwaki, A. Kuramata, H. Murakami, and Y. Kumagai, Journal of Physics D: Applied Physics **50**, 333002 (2017).
19. M. Kobata, T. Okane, K. Nakajima, E. Suzuki, K. Ohwada, K. Kobayashi, H. Yamagami, and M. Osaka, Journal of Nuclear Materials **498**, 387 (2018).
20. T. Suzuki, T. Ogata, M. Tanaka, T. Kobayashi, H. Shiwaku, T. Yaita, and H. Narita, Analytical Sciences **35**, 1353 (2019).
21. M. Simonnet, T. Kobayashi, K. Shimojo, K. Yokoyama, and T. Yaita, Inorganic Chemistry **60**, 13409 (2021).
22. T. Shobu, K. Tozawa, H. Shiwaku, H. Konishi, T. Inami, T. Harami, and J. Mizuki, AIP Conference Proceedings **879**, 902 (2007).
23. C. Kalha, N.K. Fernando, P. Bhatt, F.O. Johansson, A. Lindblad, H. Rensmo, L.Z. Medina, R. Lindblad, S. Siol, L.P. Jeurgens, C. Cancellieri, K. Rossnagel, K. Medjanik, G. Schönhense, M. Simon, A.X. Gray, S. Nemšák, P. Lömker, C. Schlueter, and A. Regoutz, Journal of Physics: Condensed Matter **33**, 233001 (2021).
24. J. Tang and Y. Yamashita, ACS Applied Electronic Materials **3**, 4618 (2021).
25. Y. Tsai, J. Tang, and Y. Yamashita, ACS Applied Electronic Materials **5**, 3843 (2023).
26. I. Alperovich, D. Moonshiram, A. Soldatov, and Y. Pushkar, Solid State Communications **152**, 1880 (2012).
27. M. Roy and S.J. Gurman, Journal of Synchrotron Radiation **8**, 1095 (2001).
28. E. Bosman and J. Thieme, Journal of Physics: Conference Series **186**, 012004 (2009).
29. K. Nakanishi and T. Ohta, Journal of Physics: Condensed Matter **21**, 104214 (2009).

30. J.J. Rehr, J.J. Kas, F.D. Vila, M.P. Prange, and K. Jorissen, Physical Chemistry Chemical Physics **12**, 5503 (2010).
31. V. Jain, M.C. Biesinger, and M.R. Linford, Applied Surface Science **447**, 548 (2018).
32. J. Végh, Journal of Electron Spectroscopy and Related Phenomena **151**, 159 (2006).
33. J.E. Castle and A.M. Salvi, Journal of Vacuum Science & Technology A: Vacuum, Surfaces, and Films **19**, 1170 (2001).
34. H. Masaharu, SPring-8/SACLA Research Report **3**, 403 (2015)
35. 1 E. Pehlke and M. Scheffler, Physical Review Letters **71**, 2338 (1993).
36. A.X. Gray, C. Papp, S. Ueda, B. Balke, Y. Yamashita, L. Plucinski, J. Minár, J. Braun, E.R. Ylvisaker, C.M. Schneider, W.E. Pickett, H. Ebert, K. Kobayashi, and C.S. Fadley, Nature Materials **10**, 759 (2011).
37. A.J. Berry, H.St.C. O'Neill, K.D. Jayasuriya, S.J. Campbell, and G.J. Foran, American Mineralogist **88**, 967 (2003).
38. S.T. Barlow, D.J. Bailey, A.J. Fisher, M.C. Stennett, C. Gausse, H. Ding, V.A. Krasnov, S.Y. Sayenko, N.C. Hyatt, and C.L. Corkhill, Npj Materials Degradation **4**, (2020).
39. B. Kosog, H.S. La Pierre, M.A. Denecke, F.W. Heinemann, and K. Meyer, Inorganic Chemistry **51**, 7940 (2012).
40. L. Qiao, H.Y. Xiao, S.M. Heald, M.E. Bowden, T. Varga, G.J. Exarhos, M.D. Biegalski, I.N. Ivanov, W.J. Weber, T.C. Droubay, and S.A. Chambers, Journal of Materials Chemistry C **1**, 4527 (2013).
41. B. Ravel and M. Newville, Journal of Synchrotron Radiation **12**, 537 (2005).
42. B. Ravel and M. Newville, Physica Scripta, 1007 (2005).
43. King, R. B, *Encyclopedia of inorganic chemistry*, 2nd ed. (Wiley, New York, 2005), Vol. 10, p. 6696.
44. J.B. Varley, J.R. Weber, A. Janotti, and C.G. Van de Walle, Applied Physics Letters **97**, 142106 (2010).

Figure Captions

Fig. 1. Sn $2p_{3/2}$ core-level HAXPES spectra for (a) Sn-doped β-Ga_2O_3(001), (b) Sn metal foil, (c) SnO powder, and (d) SnO_2 powder. (a) measured at BL 22XU at SPring-8. (b)-(d) measured at PHI Quantes.

Fig. 2. (a) Normalized Sn *K*-edge XANES spectra of Sn-doped β-Ga_2O_3(001), Sn metal, SnO, and SnO_2. (b) magnified absorption edge of the Sn *K*-edge XANES spectra. (c) Sn oxidation state as a function of the energy of the absorption edge for Sn K-edge.

Fig. 3. (a) Normalized Sn *K*-edge EXAFS spectrum and (b) k^2-weighted Sn *K*-edge EXAFS for Sn-doped β-Ga_2O_3(001). Fourier transforms of the k^2-weighted EXAFS (black solid line) and the fitting results (red solid line) for Sn_{Ga} in (c) Octa site and (d) Tetra site. The fitting range was 1–2.2 Å. The amplitude reduction factor and reliability factor values for Octa Sn_{Ga} site and Tetra Sn_{Ga} site were set to 0.8, 0.026 and 0.8, 0.051, respectively. (without phase shift correction)

Fig. 4. (a) Normalized Sn *K*-edge XANES spectrum for Sn-doped β-Ga_2O_3(001). The simulated XANES spectra of (b) Octa Sn_{Ga} (red line) and (c) Tetra Sn_{Ga} (blue line) sites. In the FEFF9 simulations, the many-body amplitude reduction factor was set to 1.0. The cluster size of 9.5 Å was employed, which possessed ~350 atoms. The final state effect (Z+1 approximation) was employed for the simulations.

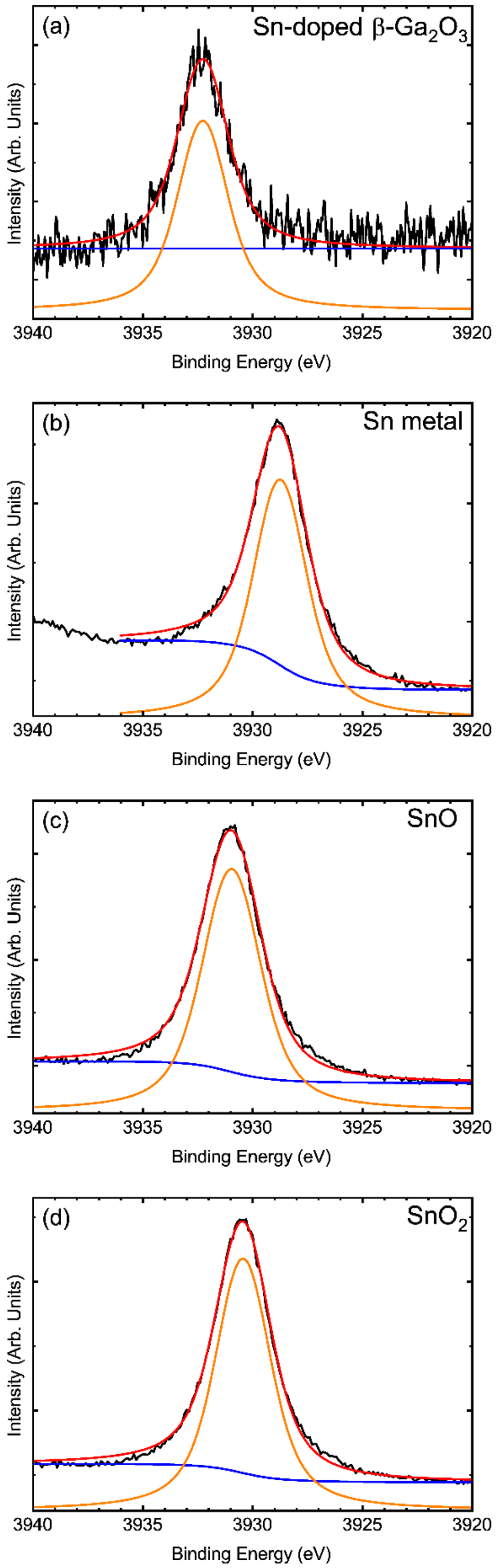
(a)
Sn-doped β-Ga$_2$O$_3$
Intensity (Arb. Units)
3940
3935
3930
3925
3920
Binding Energy (eV)
(b)
Sn metal
Intensity (Arb. Units)
3940
3935
3930
3925
3920
Binding Energy (eV)
(c)
SnO
Intensity (Arb. Units)
3940
3935
3930
3925
3920
Binding Energy (eV)
(d)
SnO$_2$
Intensity (Arb. Units)
3940
3935
3930
3925
3920
Binding Energy (eV)

Fig. 1

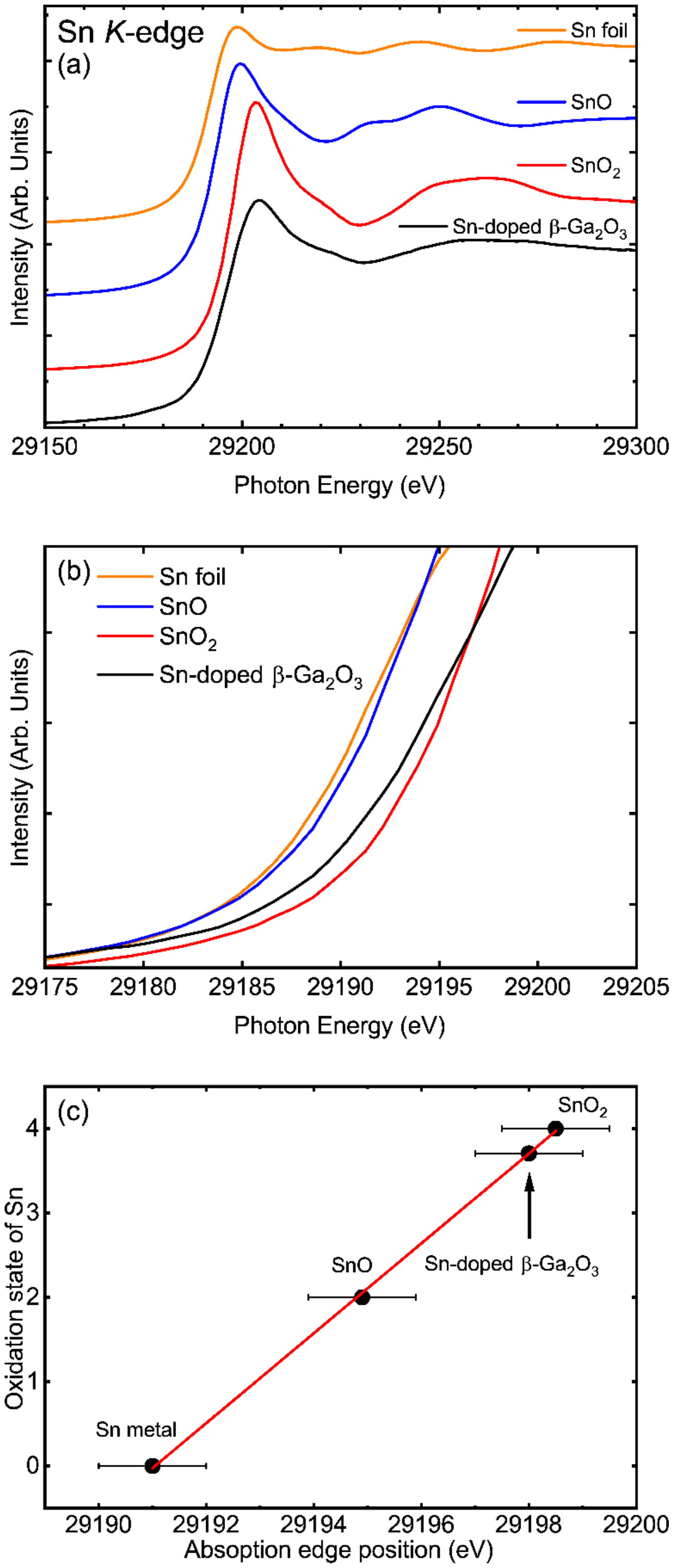
Sn K-edge
(a)
Sn foil
SnO
SnO2
Sn-doped β-Ga2O3
Intensity (Arb. Units)
29150
29200
29250
29300
Photon Energy (eV)
(b)
Sn foil
SnO
SnO2
Sn-doped β-Ga2O3
Intensity (Arb. Units)
29175
29180
29185
29190
29195
29200
29205
Photon Energy (eV)
(c)
SnO2
SnO
Sn-doped β-Ga2O3
Sn metal
Oxidation state of Sn
0
1
2
3
4
29190
29192
29194
29196
29198
29200
Absoption edge position (eV)

Fig. 2

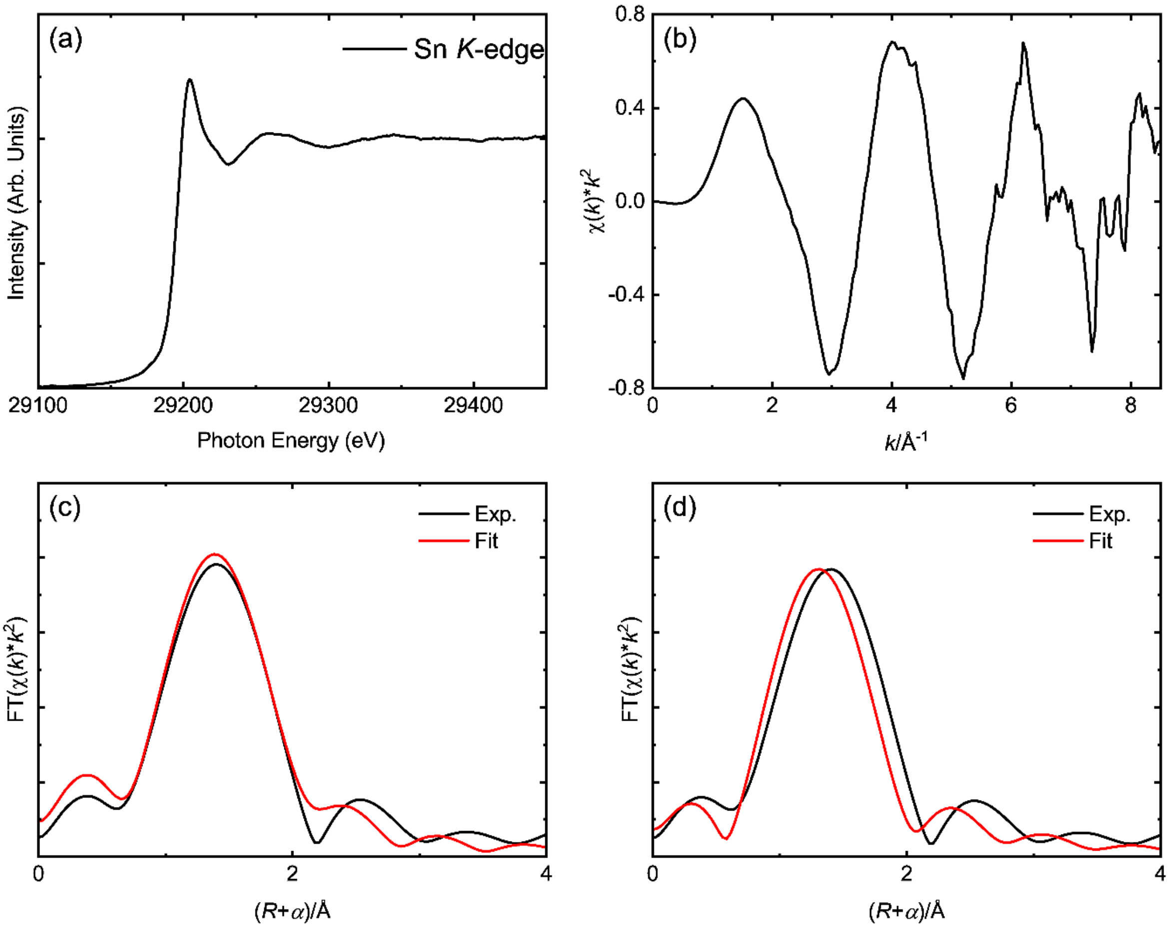
(a)
Sn K-edge
Intensity (Arb. Units)
29100
29200
29300
29400
Photon Energy (eV)
(b)
0.8
0.4
0.0
-0.4
-0.8
0
2
4
6
8
χ(k)*k²
k/Å⁻¹
(c)
Exp.
Fit
FT(χ(k)*k²)
0
2
4
(R+α)/Å
(d)
Exp.
Fit
FT(χ(k)*k²)
0
2
4
(R+α)/Å

Fig. 3

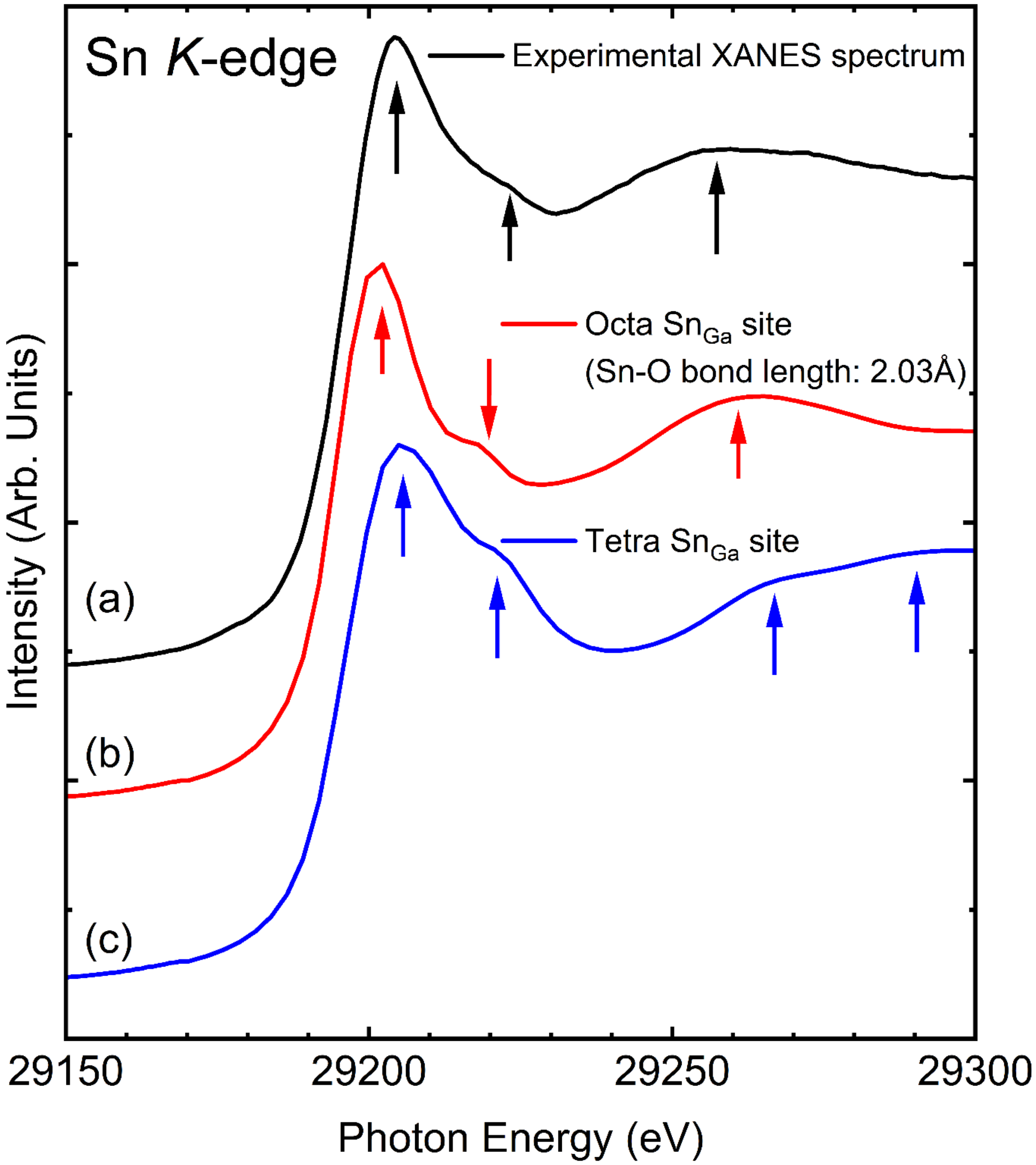
Sn *K*-edge
Experimental XANES spectrum
Octa Sn_{Ga} site
(Sn-O bond length: 2.03Å)
Tetra Sn_{Ga} site
(a)
(b)
(c)
Intensity (Arb. Units)
29150
29200
29250
29300
Photon Energy (eV)

Fig. 4